Detecting Deviations from General Relativity using Continuous Gravitational Waves

Maximiliano Isi
Mentor: Alan Weinstein
LIGO REU/Caltech SURF
Final Report
September 25, 2013

Abstract

The direct detection of a gravitational wave with the Advanced LIGO detectors provides the opportunity to measure departures from General Relativity. These departures can arise in the speed of the gravitational wave, existence of alternate polarizations and parity violation. To measure these, we can simulate a single detector measurement of a continuous gravitational wave from a well-defined pulsar source, for example the Crab pulsar, due to an asymmetry in the moment of inertia. The speed of a gravitational wave can be measured from the Doppler frequency modulation of the signal, with an accuracy that depends on the strength of the signal. We precisely quantify the achievable accuracy and compare it with other methods of measuring the "speed of gravity". Furthermore, we extend our previous analysis of gravitational wave polarizations to include new pulsars and LIGO S6 data.

Contents

1 Introduction

Since its introduction in 1915, Einstein's theory of General Relativity (GR) has been confirmed by experiment in every occasion. However, GR has not yet been tested with great precision on scales larger than the solar system or for highly dynamical gravitational fields [1]. Those kinds of rapidly changing fields can give rise to gravitational waves (GWs) –self propagating stretching and squeezing of spacetime originating in the acceleration of massive objects, like spinning neutron stars [2].

Although GWs are yet to be directly observed, detectors such as the Laser Interferometer Gravitational Wave Observatory (LIGO) expect to confirm their existence in the next 5 years, giving us a chance to probe GR on new grounds [3]. Similarly, LIGO data could also be used to test alternative theories of gravity that disagree with GR on the properties of GWs.

Deviations from GR could be observed in GW properties, such as polarization or speed. For reasons related to conservation of momentum and energy, GR allows for the existence of only two out of six possible GW polarization modes [4]. Einstein's theory also predicts GWs propagate at the speed of light, which means the graviton is massless [3]. Thus, detecting any of the alternative four polarizations or concluding gravitons have mass would directly point to physics beyond GR [4].

When looking for a weak signal in noisy LIGO data, certain physical models are used to target the search and are necessary to make any detection possible [1]. These are usually based on predictions from GR. Hence assuming an incorrect model could yield a weak detection or no detection at all. For the same reason, If GR is not a correct description for highly dynamical gravity, checking for patterns given by alternative models could result in detection where no signal had been seen before. This could potentially explain why gravitational waves have not been detected yet. If this is the case, not only the existence of gravitational waves would be confirmed, but also GR would be refuted. Thus, this project could have profound consequences for all of fundamental physics and astrophysics.

2 Polarizations

2.1 Background

Just like electromagnetic waves, GWs can present different kinds of polarizations. Most generally, there exist six possible modes: plus (+), cross ($\times$), vector x (xz), vector y (yz), breathing (b) and longitudinal (l). Their effects on a free-falling ring of particles are illustrated in Fig. 1. Transverse GWs (+, $\times$ and b) change the distance between particles separated in the plane perpendicular to the direction of propagation (taken to be the z-axis). Vector GWs are also transverse; but, because all particles in a plane perpendicular to the direction of propagation are equally accelerated, their relative separation is not changed. Nonetheless, particles farther from the source move at later times, hence varying their position relative to points with both different x-y coordinates and different z distance. Finally, longitudinal GWs change the distance between particles separated along the direction of propagation.

In reality, however, GWs might only possess some of those components: different theories of gravity predict the existence of different polarizations. In fact, + and $\times$ are associated with tensor theories, xz and yz with vector theories, and b and l with scalar theories. In terms of particle physics, this differentiation is also linked to the predicted helicity of the graviton: ± 2, ± 1 or 0, respectively. Consequently, GR only allows + and $\times$, while scalar-tensor theories also predict the presence of some extra b component whose strength depends on the source [4]. A more extreme example, Carver Mead's Four-Vector Gravity (G4v) claims to reproduce all the predictions of GR, including weak-field tests, total radiated power of GWs and frequency modulation. However, this purely vector theory differs widely with GR when it comes to gravitational wave polarizations [5]. Thus, the only way to test G4v would be to detect xz and yz modes instead of + and $\times$.

Note that, because of their symmetries, the breathing and longitudinal modes are degenerate for interferometric detectors, so it is enough to just consider one of them in the analysis. Also, we assume other properties of the waves, such as frequency or speed, remain constant across modes. This restricts the detectable differences between polarizations to amplitude modulation.

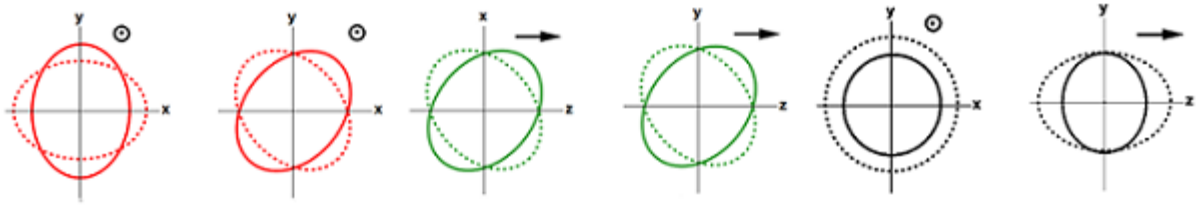

Figure 1: Illustration of the effect of different GW polarizations on a ring of test particles. +, × tensor modes (red); xz, yz vector modes (green); and b, l scalar modes (black). In all of these diagrams the wave propagates in the z-direction [4].

2.1.1 Signal

Because of their simplicity and periodicity, continuous waveforms (CGWs) are one of the best resources to study GW polarizations. These GWs are quasi-sinusoidal and present well-defined frequencies (usually, twice the rotational frequency of the source). Because of this, continuous signals can be integrated over long periods of time, thus improving the likelihood of detection. Furthermore, CGWs are produced by sources with periodic motion, such as binary systems or spinning neutron stars [6]. Such sources can be precisely localized, which simplifies the search.

Simulation of a CGW is straightforward. The general form of a such signal is:

$$h(t) = \sum_p F_p(t;\psi|\alpha,\delta,\lambda,\phi,\gamma,\xi)\ h_p(t;\iota,h_0,\phi_0,\nu,\dot{\nu},\ddot{\nu}) \tag{1}$$

where F_p is the detector sensitivity (antenna pattern) and h_p a sinusoidal waveform with same frequency as the GW for the polarization p. The detector parameters are: λ, longitude; ϕ, latitude; γ, angle of the detector arm measured from East; and ξ, the angle between arms. Values for the LIGO and Virgo detectors are shown in Table 1. The source parameters are: ι, the inclination of the pulsar; h_0, an overall amplitude factor dependent on the source; ϕ_0, a phase offset; ν, the rotation frequency; and finally $\dot{\nu}$ and $\ddot{\nu}$ the first and second derivatives. Also, α is the right ascension and δ the declination of the pulsar in celestial coordinates (ICRS).

Table 1: LIGO detectors [7]

	LHO	LLO	VIR
Latitude (λ)	46.45°	30.56°	43.63°
Longitude (ϕ)	-119.41°	-90.77°	10.5°
Orientation (γ)	126.0°	197.7°	71.5°

We have generated our own antenna patterns for the Hanford (LHO) and Livingston (LLO) detectors numerically by describing the wave and interferometer vectors in celestial coordinates ($[w_x, w_y, w_z]$ and $[d_x, d_y, d_z]$, respectively). Knowing that the different polarizations act through the following strain tensors:

$$e^{+}_{jk} = \begin{pmatrix} 1 & 0 & 0 \\ 0 & -1 & 0 \\ 0 & 0 & 0 \end{pmatrix} \qquad e^{\times}_{jk} = \begin{pmatrix} 0 & 1 & 0 \\ 1 & 0 & 0 \\ 0 & 0 & 0 \end{pmatrix} \tag{2,3}$$

$$e^{l}_{jk} = \sqrt{2}\begin{pmatrix} 0 & 0 & 0 \\ 0 & 0 & 0 \\ 0 & 0 & 1 \end{pmatrix} \qquad e^{b}_{jk} = \begin{pmatrix} 1 & 0 & 0 \\ 0 & 1 & 0 \\ 0 & 0 & 0 \end{pmatrix} \tag{4,5}$$

$$e^x_{jk} = \begin{pmatrix} 0 & 0 & 1 \\ 0 & 0 & 0 \\ 1 & 0 & 0 \end{pmatrix} \qquad e^y_{jk} = \begin{pmatrix} 0 & 0 & 0 \\ 0 & 0 & 1 \\ 0 & 1 & 0 \end{pmatrix} \tag{6,7}$$

and letting the response be $(dx - dy)/2L$, one can easily compute the corresponding dyadic products to obtain the antenna patterns [8]:

$$A_+ = (w_x \cdot d_x)^2 - (w_x \cdot d_y)^2 - (w_y \cdot d_x)^2 + (w_y \cdot d_y)^2 \tag{8}$$

$$A_\times = 2(w_x \cdot d_x)(w_y \cdot d_x) - 2(w_x \cdot d_y)(w_y \cdot d_y) \tag{9}$$

$$A_b = (w_x \cdot d_x)^2 - (w_x \cdot d_y)^2 + (w_y \cdot d_x)^2 - (w_y \cdot d_y)^2 \tag{10}$$

$$A_l = (w_z \cdot d_x)^2 - (w_z \cdot d_y)^2 \tag{11}$$

$$A_{xz} = 2(w_x \cdot d_x)(w_z \cdot d_x) - 2(w_x \cdot d_y)(w_z \cdot d_y) \tag{12}$$

$$A_{yz} = 2(w_y \cdot d_x)(w_z \cdot d_x) - 2(w_y \cdot d_y)(w_z \cdot d_y) \tag{13}$$

This way, by accounting for the change in the arm vectors due to the rotation of the Earth, we are able to compute the detector sensitivity at any moment in time (Fig. 2). We have verified that the patterns obtained this way are identical to those officially accepted by the LIGO Scientific Collaboration [9].

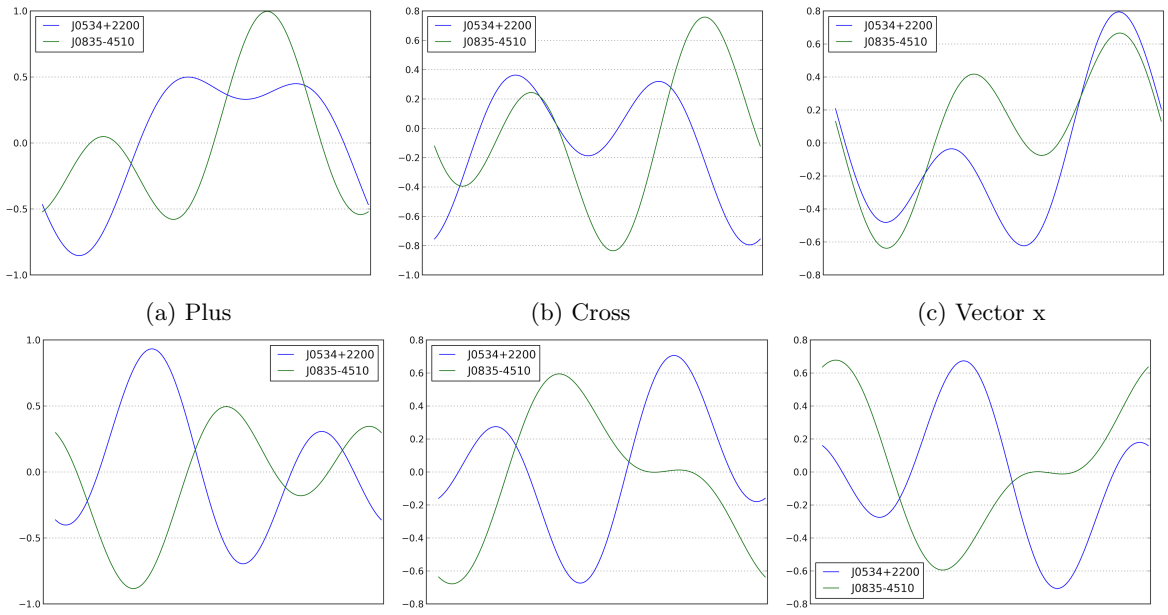

(a) Plus (b) Cross (c) Vector x

(d) Vector y (e) Breathing (f) Longitudinal

Figure 2: LHO response to different polarizations from the Crab (PSR J0534+2200) and Vela (PSR J0835-4510) pulsars over from 00:00 UTC to 24:00 UTC.

2.1.2 Data reduction

Polarizations can only be distinguished by their antenna patterns, hence we are only concerned with the amplitude modulation of the signal. Accordingly, it suffices to consider a narrow frequency band of the data, heterodyned around the expected frequency of CGW from a particular source. When performing this

heterodyne one must be careful to account for the phase evolution of the signal due to frequency derivatives and Einstein, Roemer and Shapiro time delays [10, 6]. To make the data more manageable, they are put through a low-pass Butterworth filter so they can be averaged in minute-long time bins [10, 6] without information loss. Such a reduction of the data extremely simplifies our analysis. Note that this process, especially the corrections for timing delays, requires great care and expertise; we are grateful to the experts who prepared these heterodyned data.

After undergoing through the aforementioned process, the data B_k for the k^{th} minute-long time bin (often labeled by GPS time of arrival) are of the form:

$$B(t_k) = \sum_{p=1}^{5} a_p F_p(t_k) + n(t_k) \tag{14}$$

where F_p is the detector amplitude response for polarization p at time t_k, a_p is a time-independent, complex factor representing the contribution of such polarization to the whole signal, and $n(t_k)$ is the heterodyned and averaged complex noise in bin k (following [10]). As previously mentioned, the breathing and longitudinal polarization are indistinguishable for the detectors, so we just loop over five values of p.

2.2 Analysis

2.2.1 Search methods

Following our previous work [11] [12], we perform χ^2 regressions (analogous to matched filtering) to model dependent and independent templates . This way we attempt to recover the presence of each polarization, represented by the amplitude of the corresponding a_p complex-valued factor recovered by the minimization. To improve efficiency and reliability, the regression is performed by means of an SVD decomposition.

When a particular theory is assumed (viz GR or G4v), the search is considered model dependent and the weights predicted by the theory (usually a function of ι when non-zero) are added to each antenna pattern so that we can extract a real number h_{rec} representative of the overall "strength" of the recovered signal. Although we rescale the amplitudes, we do not constraint the phase differences between components, since the χ^2-minimization is able to fit for the phase too and the results of the search are unchanged by any initial phase offsets.

In the case of model independent searches, when the a_p's are not rescaled or forced to have any particular phase difference, h_{rec} is taken to be the norm of $\mathbf{a} = [a_p]_{p=0}^{4}$. A search of this kind, which makes use of all the 5 non-degenerate antenna patterns, is equivalent to a regression to the *sidereal* basis set

$$\{1,\ \cos\omega,\ \cos 2\omega,\ \sin 2\omega,\ \sin 2\omega\} \tag{15}$$

where ω is the sidereal rotational frequency of the Earth. This is an orthogonal basis which spans the space of the antenna patterns. We showed in [11] that results of regressions to these two bases sets yield exactly the same significance and coefficients can be converted back and forth between the two by use of a coordinate transformation matrix.

As outlined in [11], the significance of the fit is evaluated through the covariance matrix C. This can be computed by taking the inverse of $A^T A$, where A is the design matrix of the system. In particular, we define the significance of the fit (signal SNR) as

$$s = \sqrt{\mathbf{a}^\dagger C^{-1} \mathbf{a}} \tag{16}$$

where † indicates Hermitian conjugation.

Knowledge of source parameters is necessary to simulate a particular CGW signal and perform the search. Unfortunately, there are very few pulsars for which we possess accurate measurements of inclination and polarization angles (Table 2), and the list is further reduced when one requires the potential GW frequency to be in the range of present interferometric detectors. When performing searches, we marginalize over the uncertainty ranges of location and orientation values obtained from the ATNF Pulsar Catalog [13]. Such

Table 2: Known axis polarization (ψ) and inclination (ι) angles [14].

	ψ (deg)	ι (deg)
Crab	124.0	61.3
Vela	130.6	63.6
J1930+1852	91	147
J2229+6114	103	46
B1706−44	163.6	53.3
J2021+3651	45	79

	ψ (deg)	ι (deg)
J0205+6449	90.3	91.6
J0537−6910	131	92.8
B0540−69	144.1	92.9
J1124−5916	16	105
B1800−21	44	90
J1833−1034	45	85.4

information is absent for the majority of candidate sources and we must then marginalize over the broad ranges of $[-\pi/4, \pi/4]$ and $[-1, 1]$ for ψ and $\cos\iota$ respectively [6] [10].

In order to obtain upper limits for the strength of signals potentially buried in the data, we first make use of several instantiations of fabricated data in which we inject signals of different strengths. This allows us to define a noise background, determined by the maximum false positive, above which we can declare a detection with certain confidence. The instantiations on which we inject and search for signals are generated by re-heterodyning original LIGO or Virgo data at different frequencies. This shifts the phases of the reduced data, eq. (14), effectively removing all traces of any potential signal and making the analysis blind to the presence of a signal. For GR and G4v signals, injections can be constructed with a $+\pi/2$ (*GRp*, *G4vp*) or a $-\pi/2$ (*GRm*, *G4vm*) phase difference between the $+$, $\times$ and xz, yz components respectively.

The above is carried out by means of plots like those in Fig. 3, which present the detection significance 16 vs. injection strength: the red marks at $h_{inj} = 0$ correspond to the background instantiations and those at $h_{inj} > 0$ are injection trials to assess recovery success for different strenghts by different search templates. Also, Fig. 4 shows similiar plots for the reconstructed strength (h_{rec}) of the injected signals.

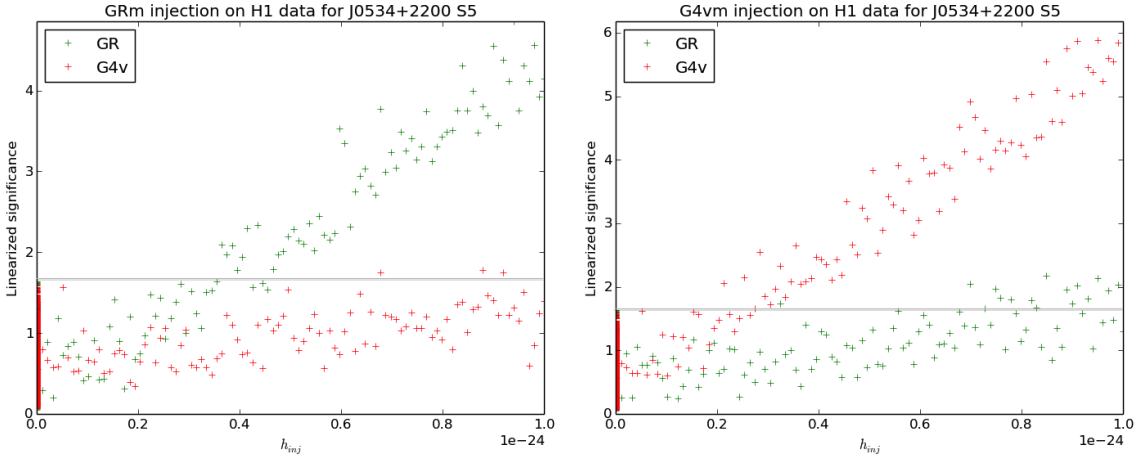

(a) GR injections

(b) G4v injections

Figure 3: LIGO H1 S5 Crab significance curves, as defined in eq. (16): GR (left) and G4v (right) injections. Color corresponds to the template used for recovery: GR (green) or G4v (red).

2.2.2 Candidate sources

Two of the best known sources are the Crab (PSR J0534+2200) and Vela (PSR J0835-4510) pulsars, for which we do not only possess accurate timing data from radioastronomy (Tables 3-6), but also orientation information from X-ray observations (Figs. 5, 6). In the case of the Crab, we extend our study in [11] to look

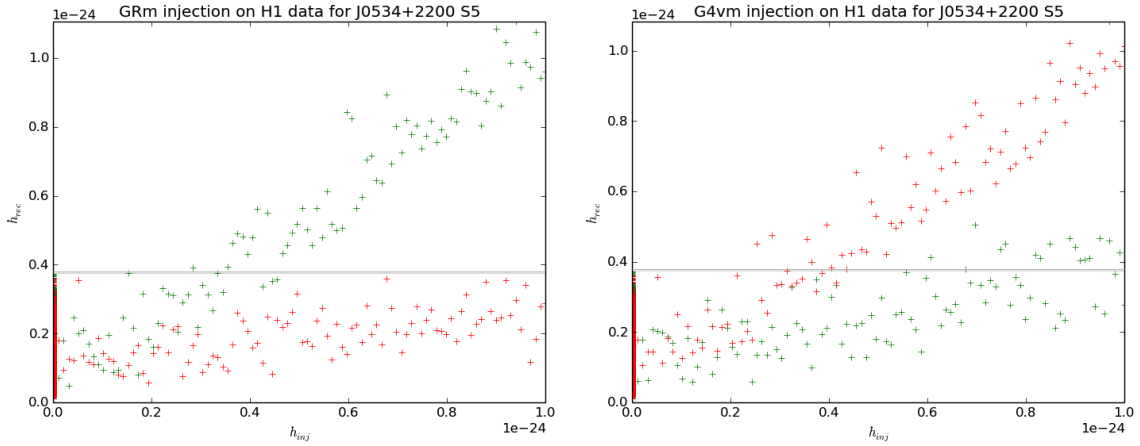

(a) GR injections

(b) G4v injections

Figure 4: LIGO H1 S5 Crab recovered strength curves: GR (left) and G4v (right) injections. Color corresponds to the template used for recovery: GR (green) or G4v (red).

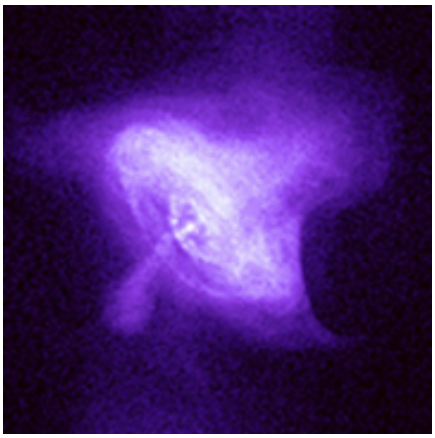

Figure 5: X-ray image of the Crab pulsar (NASA/CXC/MSFC/M.Weisskopf et al).

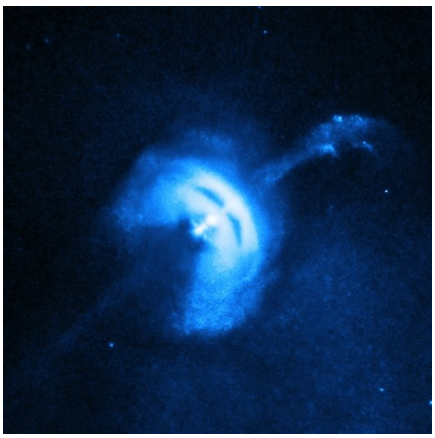

Figure 6: X-ray image of the Vela pulsar (NASA/CXC/Univ of Toronto/M.Durant et al).

at not only at LIGO S5, but also S6 data; while for Vela we use Virgo VSR2 and VSR4 data. A comparison of the heterodyned data standard deviations taken over day-long segments for each run can be seen in Fig. 7.

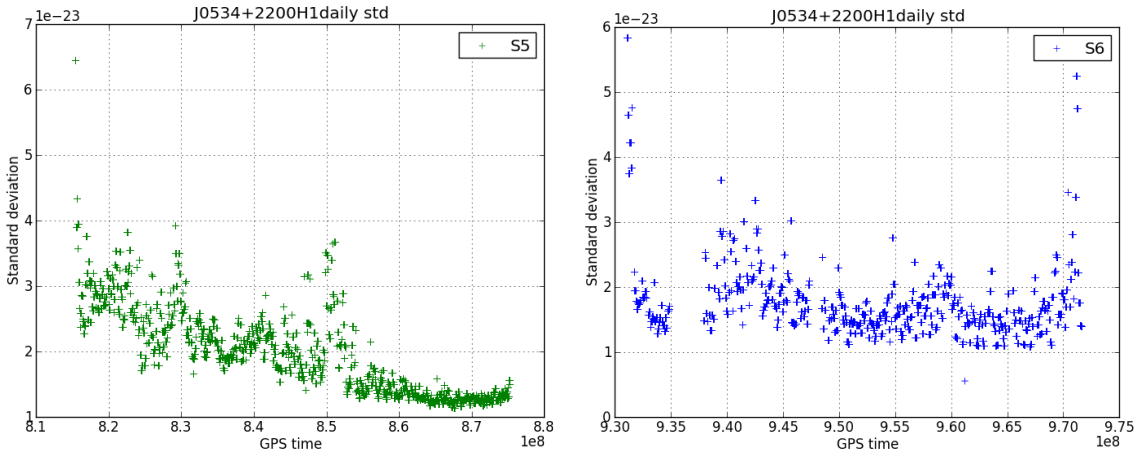

(a) S5 (b) S6

Figure 7: Daily standard deviation of S5 (left) and S6 (right) H1 data heterodyned for the Crab pulsar.

Besides those two well-studied pulsars, we analyzed LIGO H1 data prepared for 129 other potential sources. Injections and searches on these were carried out by choosing random values of orientation and inclination parameters as outlined in the previous section and marginalizing over those angles when computing the detection significance. All these data were made available to us thanks to Matthew Pitkin from the University of Glasgow.

Table 3: Crab pulsar parameters [13].

Right ascension (α)	83.65°
Declination (δ)	22°
Polarization angle (ψ)	125.15°
Inclination angle (ι)	62°
GW frequency	59.4 Hz

Table 4: Crab rotational frequency [16].

ν	29.7 Hz
$\dot{\nu}$	-3.71×10^{-10} Hz/s
$\ddot{\nu}$	1.24×10^{-20} Hz/s^2
Epoch	MJD 40675

Table 5: Vela pulsar parameters [13][15].

Right ascension (α)	128.83°
Declination (δ)	-45.83°
Polarization angle (ψ)	130.63°
Inclination angle (ι)	63.6°
GW frequency	22.38 Hz

Table 6: Vela rotational frequency [15].

ν	11.19 Hz
$\dot{\nu}$	-1.56×10^{-11} Hz/s
$\ddot{\nu}$	4.91×10^{-22} Hz/s^2
Epoch	MJD 54620

2.3 Results

Previous results for Crab H1 S5 data have been successfully reproduced by new, corrected routines, as shown in Fig. 3 (cf. [11]). Indeed, we are able to detect signals using model independent and dependent methods

with equal efficiency and we confirm that assuming the wrong model significantly decreases the likelihood of detection.

Making use of S5 we can retrieve signals of $h_0 \approx 2 \times 10^{-25}$ and greater with high significance. This can be compared to the results corresponding to the shorter LIGO S6 run, for which the minimum h_{inj} detected is a generally factor of 2 bigger than for S5 (Fig. 8). Plots for Vela Virgo VSR4 data are presented in Fig. 9. Although this is by far the best of the two runs, the results are almost an order of magnitude worse than for the Crab.

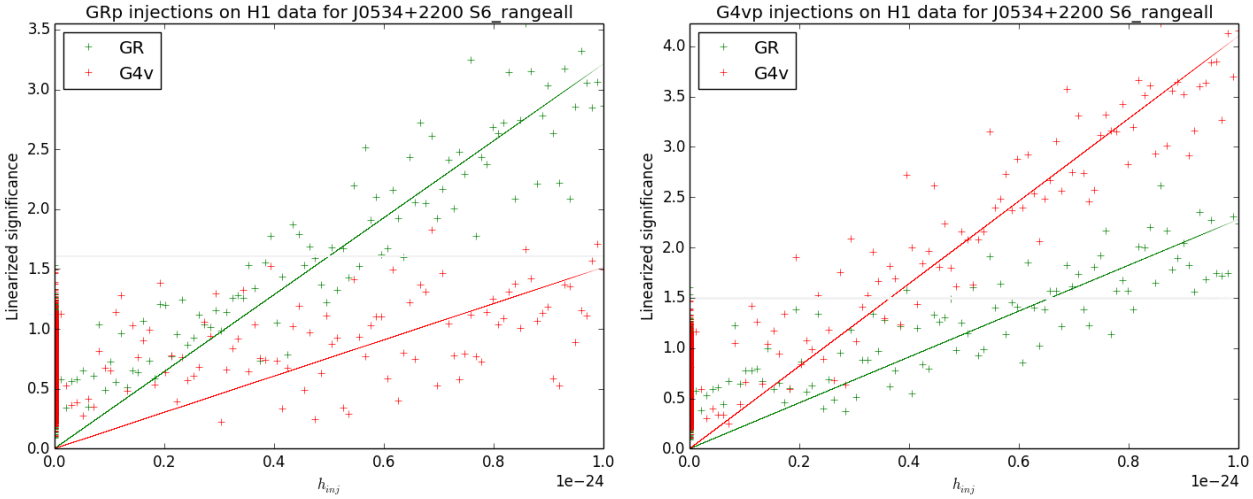

(a) GR injections

(b) G4v injections

Figure 8: LIGO H1 S6 Crab significance curves, as defined on eq. (16): GR (left) and G4v (right) injections. Color corresponds to the template used for recovery: GR (green) or G4v (red). The solid lines are the result of a least-square fit forcing null y-intersect. Their slope reflects the performance of the template at picking up the signal.

Results for the remaining 129 pulsars for which we possess H1 data are summarized in the histograms of Figs. 10, 11. The plots of Fig. 10 consist of histograms of the interpolated value of injection strength(h_{inj}) for which the linear fit to the recovered signal significances (solid lines in Figs. 8, 9) intersects the noise level line (gray line in Figs. 8, 9). This can be taken as a measure of the performance of each template at recovering signals of certain kind, since a smaller the intersection value the more sensitive the search. In the absence of a signal, this is approximately the upper limit that can be placed on the signal strength at 95% confidence level (above 95% of the noise instantiations). However, the intersection value depends also on the quality of the data (noise amplitude) at the heterodyned frequency, and not only on the templates themselves. Note that the best results (smaller intersection) are obtained when the search template matches the injection, and the model independent search is practically as good as the matching model.

Similarly, Fig. 11 shows results for the slope of the linear fits (solid lines in Figs. 8, 9) of recovered signal significance: the significance or SNR is proportional to the injected signal strength for a given source and detector. Again, this shows recovery success for different templates, since a steeper line is indicative of higher sensitivity. Interestingly, histograms for both kinds of injections seem to show an almost exact correspondence between the results of model independent searches and those assuming the model matching the injections Thus, the model independent search is as effective as a GR- or G4v-specific search, independent of the true polarization of the wave.

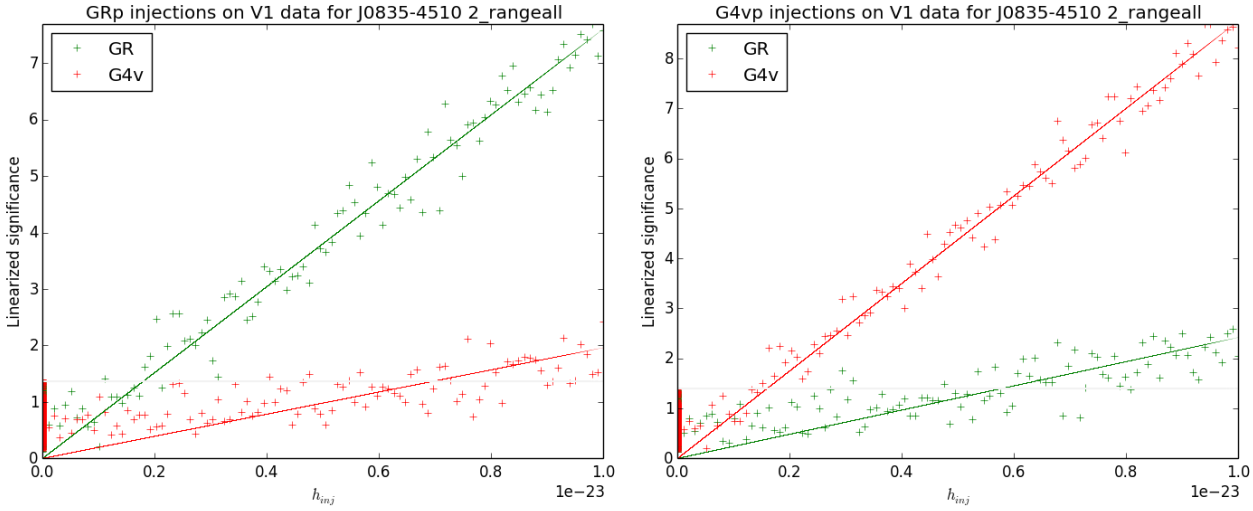

(a) GR injections

(b) G4v injections

Figure 9: Virgo V1 VSR4 Vela significance curves, as defined on eq. (16): GR (left) and G4v (right) injections. Color corresponds to the template used for recovery: GR (green) or G4v (red). The solid lines are the result of a least-square fit forcing null y-intersect. Their slope reflects the performance of the template at picking up the signal.

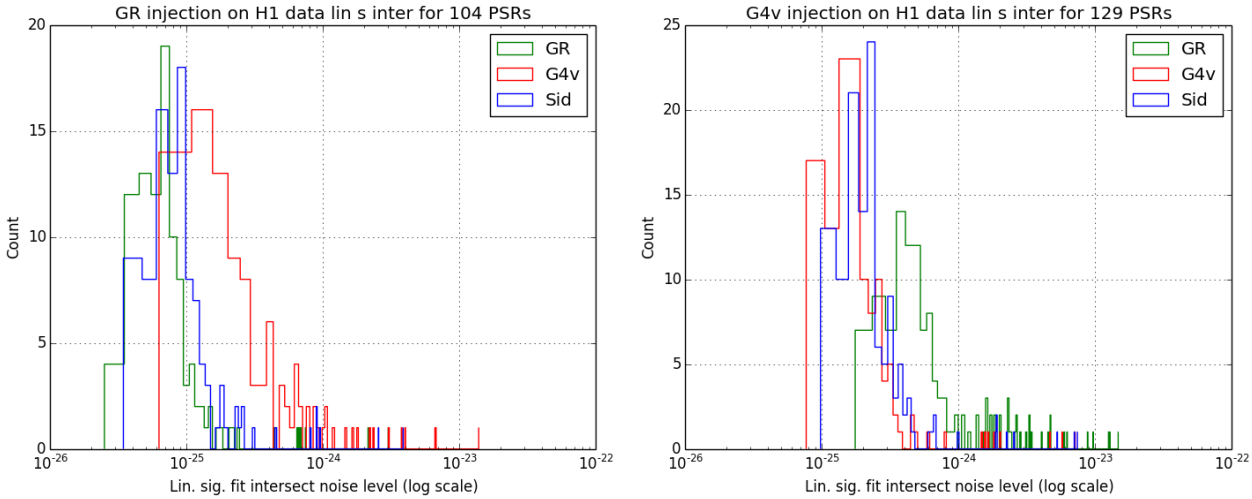

(a) GR injections

(b) G4v injections

Figure 10: Intersection between least-squares fit of recovered signal significance with corresponding noise line (cf. Figs. 8, 9) for H1 data prepared for 129 pulsars with GR (left) and G4v (right) injections. Color corresponds to the template used for recovery: GR (green), G4v (red) or model independent (blue). A smaller intersect indicates more sensitivity.

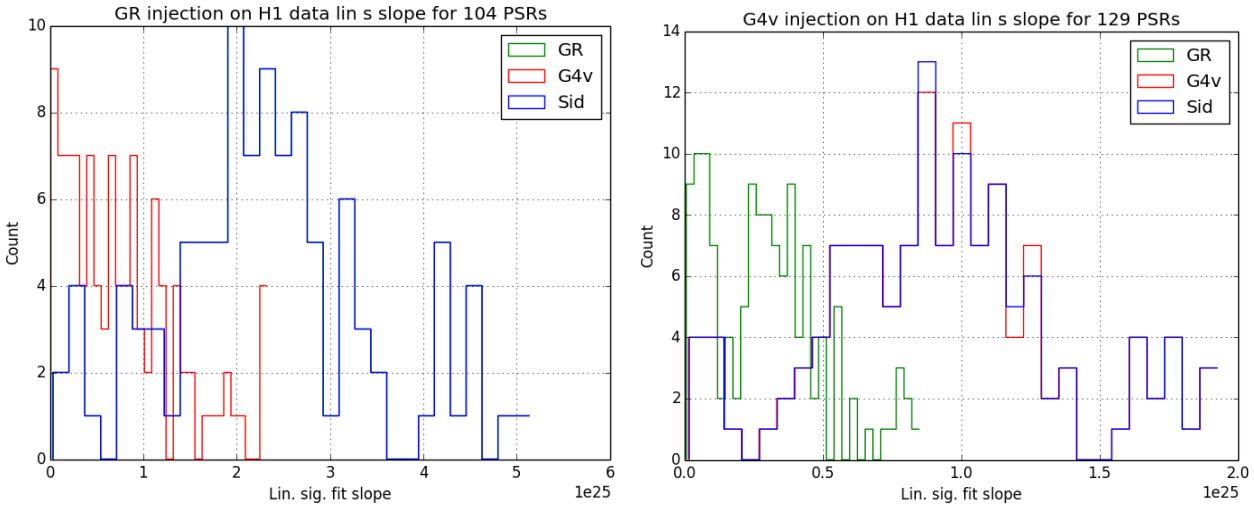

(a) GR injections

(b) G4v injections

Figure 11: Slope of least-squares fit of recovered signal significance(solid line in Figs. 8, 9) for H1 data prepared for 129 pulsars with GR (left) and G4v (right) injections. Color corresponds to the template used for recovery: GR (green), G4v (red) or model independent (blue). A larger slope indicates more sensitivity. Note that the blue curve overlays the green and red curves on plots (a) and (b) respectively.

3 Speed

3.1 Background

Although GR predicts that GWs propagate at the speed of light (i.e. $c_g = c$), it is possible that this is not the case. For example, all massive graviton theories require $c_g < c$: the relation between the mass of the graviton and the GW speed can be obtained through the dispersion relation for the graviton. From the relativistic expression for the energy of the graviton,

$$E_g = \left(m_g c^2\right)^2 + \left(p_g c\right)^2 \ , \tag{17}$$

where E_g, m_g and p_g are respectively the graviton energy mass and momentum, and the de Broglie relations

$$E_g = \hbar \omega_g \ , \tag{18}$$

$$p_g = \hbar k_g \tag{19}$$

with ω_g the angular frequency and k_g the wavenumber of the graviton wave, we obtain an expression for the group velocity of the wave packet

$$c_g \equiv \frac{d\omega_g}{dk_g} = \frac{c}{\sqrt{1 + \left(m_g c/\hbar k_g\right)^2}} \ . \tag{20}$$

Through this relation, limits on m_g can be translated into limits on c_{gw}. The most stringent bound on the graviton mass, as reported by the Particle Data Group, is $m_g < 7 \times 10^{-32}$ eV [17]. For a GW coming from the Crab, for example, this translates into

$$c - c_g \approx 4 \times 10^{-26} \mathrm{m/s} \ . \tag{21}$$

This bound, however, was derived using weak lensing, which is a static phenomenon and may not apply to the case at hand. A more relevant limit of $m_g < 7.6 \times 10^{-20}$ eV was obtained from the orbital decay rates of pulsars PSRB1913+13 and PSRB1534+12 [17]. For the case of the Crab, this means

$$c - c_g \approx 1.5 \times 10^{-15}\text{m/s} \ , \tag{22}$$

so the potential speed deviations are small.

Besides massive graviton theories, some models with extra dimensions also require $c_{gw} < c_{em}$ [18]. Measuring GW speed directly would be an excellent way to test these theories and others. To study deviations from GR in GW polarizations it is enough to consider only the amplitude modulation of the waves. However, information about the gravitational wave speed is contained in the phase evolution of the signal; thus, variations in the complex phase of the data must be carefully studied. Here we study the effect of GW speed on CGWs with GR polarization only.

3.1.1 Delays

The arrival of a GW signal to a detector is recorded in the observatory frame, which is not an inertial frame with respect to the source. Therefore, the signal of a GW is modulated by Doppler and relativistic effects; following [6], we can implement this through a time-of-arrival function:

$$t_b = t + \Delta_R + \Delta_E + \Delta_S \tag{23}$$

where Δ_R is the Roemer delay, Δ_E the Einstein delay and Δ_S the Shapiro delay. Equation (23) effectively transforms detector time t into solar system barycenter (SSB) time t_b, which is assumed to be inertial with respect to the source [19].

The Einstein delay Δ_E is caused by relativistic time dilation around the SSB and redshifting between the observatory and the geocenter. This can be written as a time-dilation integral plus a term encoding redshift effects [19] [20] :

$$\Delta_E = \frac{1}{c^2}\int_{t_0}^{t}\left(\sum_i \frac{GM_i}{|r_\oplus - r_i|} + \frac{v_\oplus^2}{2}\right)dt + \frac{\vec{s}\cdot\vec{v_\oplus} + W_0 t}{c^2} \tag{24}$$

where $r_\oplus$ is barycentric location of the geocenter, $v_\oplus$ is the Earth's barycentric velocity, and $\Delta L_c \approx 1.48 \times 10^{-8}$ and $t_0 = 43144.0003725$ (common epoch) are constants. The sum is over all bodies in the solar system except the Earth. Finally, $\vec{r}$ is the geocentric location of the observatory and $W_0 \approx 6.97 \times 10^{-10}c^2$ is the plus spin potential of the Earth at the geoid [19].

Accounting for Δ_E can be seen as a conversion from terrestial time (TT) to barycentric time (TDB): the first term in (24) accounts for the difference between geocentric coordinate time (TCG) and TDB, while the second term relates TT to TCG. Note, however, that the term *Einstein delay* is sometimes refers exclusively to the integral in (24) and not the whole expression (c.f. [21]). Although this delay can amount up to 15 s, it is almost constant and we can neglect it in our analysis [10].

The Shapiro delay Δ_S accounts for the bending of light due to the curvature of space around the SSB. To first order, this delay is a sum of the effect caused by each body i in the solar system [19]

$$\Delta_S = -\sum_i \frac{2GM_i}{c^3}\ln|r_i|(1-\cos\theta_j) \tag{25}$$

where M_j, r_j θ_j are respectively is the mass, distance to the detector and object-detector-source angle of the j^{th} object at a certain time. Higher order terms need only be considered when the source is extremely close to the solar system [19]. Because the Sun is the most massive object in the system, we can estimate the magnitude of (25) by computing this contribution only, i.e.

$$\Delta_S \approx -\frac{2GM_\odot}{c^3}\ln(1-\hat{R}\cdot\hat{x}) \tag{26}$$

with $M_\odot$ the solar mass, $\hat{R}$ the unit vector pointing from the detector to the source and and $\hat{x}$ the one pointing from the detector to Sun. Assuming that the source, the Sun and the Earth are far from being aligned and knowing that

$$G \approx 6.67 \times 10^{-11} \text{ N } (\text{m/kg})^2 \tag{27}$$

$$M \approx 1.99 \times 10^{30} \text{kg} \tag{28}$$

$$c \approx 2.7 \times 10^{8} \text{m/s} \tag{29}$$

one can estimate the magnitude of the Shapiro delay to be in the order of 10^{-7} seconds. For our purposes this is a negligible effect, since the periods of the wave we look at are of the order of milliseconds.

The Roemer (Rømer) delay is, then, the most important effect for our study. This is the time it takes the signal to travel between the detector and the SSB [19]. For a single pulsar not in a binary system, this is

$$\Delta_{R_\odot} = \frac{\vec{r} \cdot \hat{n}}{c_{gw}} \tag{30}$$

where $\vec{r}$ is the location vector of the detector with respect to the solar system barycenter, $\hat{n}$ is a unit vector pointing from the SSB towards the source and c_{gw} is the GW speed. Thus, a change in GW speed should be reflected on the Roemer delay [22].

3.1.2 Detection theory

Without taking noise into account, a continuous GR signal from a spinning or orbiting source eq. (1) , can be written as [6]:

$$s(t) = \frac{1}{2} A(t) e^{i2\phi(t_b)+\phi_0} + \frac{1}{2} \tilde{A}(t) e^{-i2\phi(t_b)-\phi_0} \tag{31}$$

$$A(t) = F_+(t) h_+ - i F_\times(t) h_\times \tag{32}$$

with F and h respectively referencing the antenna patterns and their relative strengths for the indicated polarization, and with tilde as the complex conjugation operator.

In equation (31), the source rotation frequency can be approximated by Taylor expansion

$$\phi(t_b) = 2\pi \left(\nu t_b + \frac{1}{2} \dot{\nu} t_b^2 + \frac{1}{6} \ddot{\nu} t_b^3 \right) \tag{33}$$

and, as outlined above, the extra factors in (23) can be ignored to express the detection time t_b as function of the Roemer delay $\Delta_R(t) = \frac{\vec{r}(t)\cdot\hat{n}}{c_g}$ only:

$$t_b = t + \frac{\vec{r}(t) \cdot \hat{n}}{c_g} \ . \tag{34}$$

Note that, in the equation above, the GW speed c_g does not necessarily equal the speed of light c.

Thus, the phase of the first term in (31) is

$$\varphi(t) = i4\pi \left[\nu \left(t + \frac{\vec{r}(t) \cdot \hat{n}}{c_g} \right) + \frac{1}{2} \dot{\nu} \left(t + \frac{\vec{r}(t) \cdot \hat{n}}{c_g} \right)^2 + \frac{1}{6} \ddot{\nu} \left(t + \frac{\vec{r}(t) \cdot \hat{n}}{c_g} \right)^3 + \phi_0 \right] \tag{35}$$

The data we currently possess is heterodyned at a frequency $2\phi(t_b)$ assuming $c_g = c$. If in fact this is the case, then all frequency modulation in 31 is removed by heterodyning. However, if instead $c_g \neq c$, all c_g-independent terms in equation (35) do vanish, but we are left with

$$\begin{aligned} \varphi'(t) = i4\pi \Bigg[& (\vec{r} \cdot \hat{n}) \left(\frac{1}{c_g} - \frac{1}{c} \right) \left(\nu + \dot{\nu} t + \frac{1}{2} \ddot{\nu} t^2 \right) + (\vec{r} \cdot \hat{n})^2 \left(\frac{1}{c_g^2} - \frac{1}{c^2} \right) \frac{1}{2} \left(\dot{\nu} + \ddot{\nu} t \right) \\ & + (\vec{r} \cdot \hat{n})^3 \left(\frac{1}{c_g^3} - \frac{1}{c^3} \right) \frac{1}{6} \ddot{\nu} + \phi_0 \Bigg] \end{aligned} \tag{36}$$

or, letting $\delta = \frac{c}{c_g}$ and $\Delta_{R'} = t + \frac{\vec{r}(t)\cdot\hat{n}}{c}$,

$$\varphi'(t) = i4\pi \left[\Delta_{R'} (\delta - 1) \left(\nu + \dot{\nu} t + \frac{1}{2} \ddot{\nu} t^2 \right) + \frac{1}{2} \Delta_{R'}^2 \left(\delta^2 - 1 \right) (\dot{\nu} + \ddot{\nu} t) + \frac{1}{6} \Delta_{R'}^3 \left(\delta^3 - 1 \right) \ddot{\nu} + \phi_0 \right] \tag{37}$$

Finally, after low-pass filtering, the signal takes the form:

$$s'(t) = \left[\frac{1}{2} F_+(t) h_+ - \frac{i}{2} F_\times(t) h_\times \right] e^{\varphi'(t)} \tag{38}$$

Note that that (37) is periodic over the sideral day and year and ν and its derivatives are mostly well-known constants. Remarkably, this allows us to use the data that has already been heterodyned and reduced assuming $c_{gw} = c$. In turn, therefore, we are able to detect speed variations without requiring to go back to raw LIGO data. Based on this fact, we simulate signals of different speeds and inject them into LIGO noise. We also develop search methods to detect and recover these signals.

3.2 Analysis

3.2.1 Simulation

In order to model and fit for the phase evolution of the signal, it is necessary to know the Roemer delay corresponding to the time of each data bin. In turn, this means that the location of the detector and the source with respect to the SSB must be known. In general, the position of the detector can only be obtained by consulting solar system ephemerides. These can be obtained through the HORIZONS system developed by the Solar System Dynamics Group of the Jet Propulsion Laboratory [23]. The particular ephemeris used must coincide with the one used when heterodyning (DE200 for the Crab and DE405 for the others). We make use of the files compiled by the LIGO LALSuite routine LALBarycenter ; these files can be found in ATLAS computer cluster at AEI, under the directory */usr/share/lalpulsar/* and have the added advantage of having already been time-corrected to be a function of signal arrival GPS time [21].

Once we have retrieved the location of the Earth from the ephemeris and have properly extrapolated to obtain the location at the desired time $\vec{r}_\oplus$, we can find the position of the detector in SSB coordinates by adding the vector from the geocenter to the observatory $\vec{s}$:

$$\vec{r} = \vec{r}_\oplus + \vec{s} \tag{39}$$

Clearly, $\vec{s}$ depends on the latitude and longitude of the site and varies with time as the Earth rotates in its axis over a sidereal day. Furthermore, precession and nutation of the Earth's axis should also be factored in.

The other component of the Roemer delay is the source location unit vector. In celestial coordinates (ICRS), this is given by [19]

$$\hat{n} = \hat{n}_0 + \vec{\mu}_\perp t - \left(\frac{1}{2} |\vec{\mu}_\perp|^2 \hat{n}_0 + \mu_\parallel \vec{\mu}_\perp \right) t^2 \tag{40}$$

where

$$\hat{n}_0 = \begin{pmatrix} \cos\alpha \cos\delta \\ \sin\alpha \cos\delta \\ \sin\delta \end{pmatrix} \tag{41}$$

$$\vec{\mu}_\perp = \mu_\alpha \hat{\alpha} + \mu_\delta \hat{\delta} \tag{42}$$

with

$$\hat{\alpha} = \begin{pmatrix} -\sin\alpha \\ \cos\alpha \\ 0 \end{pmatrix} \tag{43}$$

$$\hat{\delta} = \begin{pmatrix} -\cos\alpha \cos\delta \\ -\sin\alpha \cos\delta \\ cos\delta \end{pmatrix} \tag{44}$$

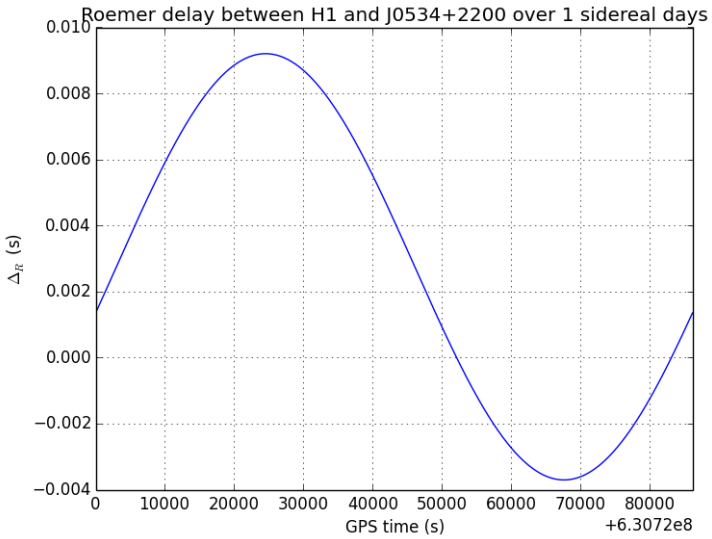

Figure 12: Roemer delay between the Crab and and LIGO H1 over 1 sidereal day.

In the preceding equations, α and δ indicate respectively the right ascension and declination of the source in ICRS. The quantities represented by μ are related to the proper motion of the source; in the case of the Crab, for instance, $\mu_\alpha = 13$ mas yr^{-1} and $\mu_\delta = 7$ mas yr^{-1} [24]. We neglect these terms due to the small magnitude of the corrections they generate.

Putting all the elements together we are able to compute eq. (30), a function with variations over a sidereal day and a sidereal year (Fig 12). Knowing this, it is straightforward to compute the phase evolution given in eq. (37) and shown in Fig. 13 for various values of δ. This, in turn, is used to compute the actual signal (Fig.14), which is needed for search and injections. Moreover, note that, as expected, changes in GW speed are manifested only in the phase evolution of the signal, and not the amplitude (Fig. 15).

3.2.2 Search

In order to quantify how well we can detect variations in GW speed, we make use of several instantiations of fabricated data into which we inject Crab H1 S6 signals corresponding to different speeds and we then try to recover the correct value of δ for different strengths of injected signal. We use both noise extracted from LIGO data and random gaussian noise of comparable standard deviation. Because we consider $c_{gw} > c_{em}$ to be unphysical, we focus mainly on the case $\delta > 1$.

The search is performed by use of matched filter: for each injection, we compute the cross-correlation between the injected data and a template for different values of potential speed parameter δ_{rec} (Fig. 16a). Of course, in the absence of noise, the match is perfect and we are able to recover the injected value of the speed parameter (δ_{inj}) flawlessly no matter what the strength of the injected signal (h_0) is (Fig. 16b). When noise is present, the quality of the match depends on the SNR.

3.3 Results

The results of the analysis for different injection strengths are shown in Fig. 17. For a strong enough signal, we are able to recover all values of δ_{inj} quite well. However, when the signal is of the order of the noise (standard deviation 10^{-23}), the peak-finding method fails and returns the values at the boundaries of the search range (horizontal lines in Fig. 17). Note that LIGO data does not seem to behave significantly different from Gaussian noise.

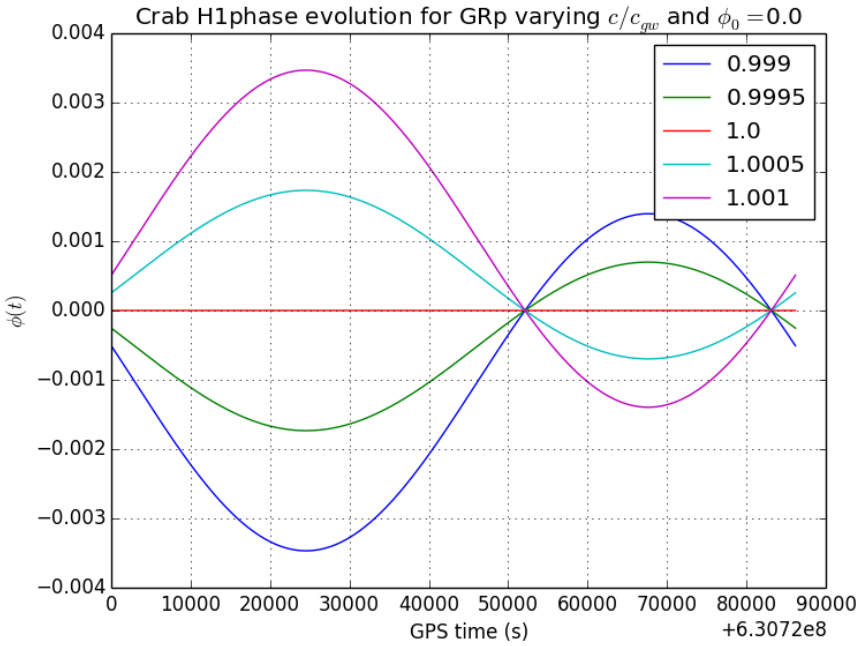

Figure 13: Phase evolution of signal (radians) over one sidereal day for different δ after heterodyning, eq. (37). As described in §2.1.2, when $\delta = 1$, i.e. $c_{gw} = c_{em}$, the phase is constant (red).

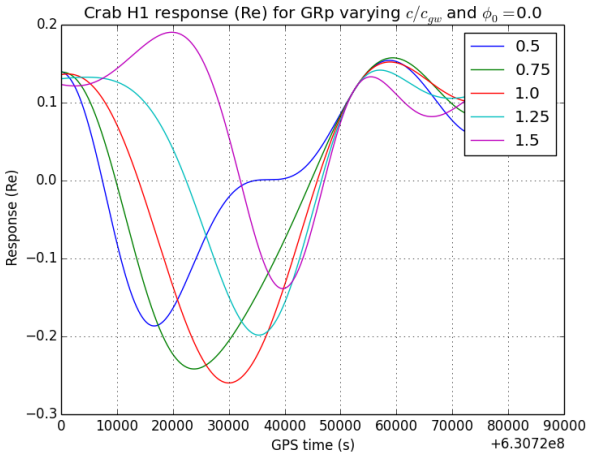

(a) Real

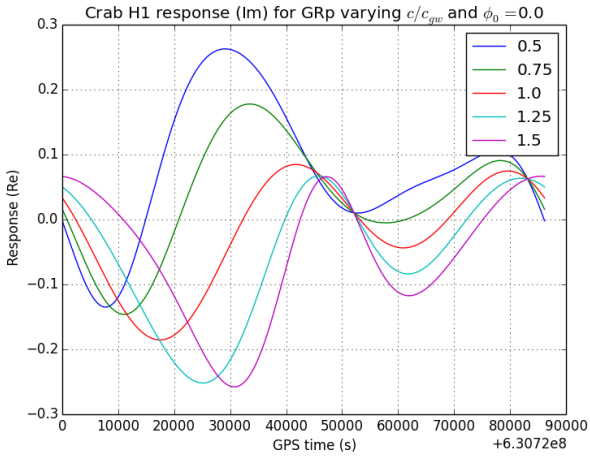

(b) Imaginary

Figure 14: Crab H1 heterodyned signal eq. (38), real (left) and imaginary (right) parts, for different values of δ.

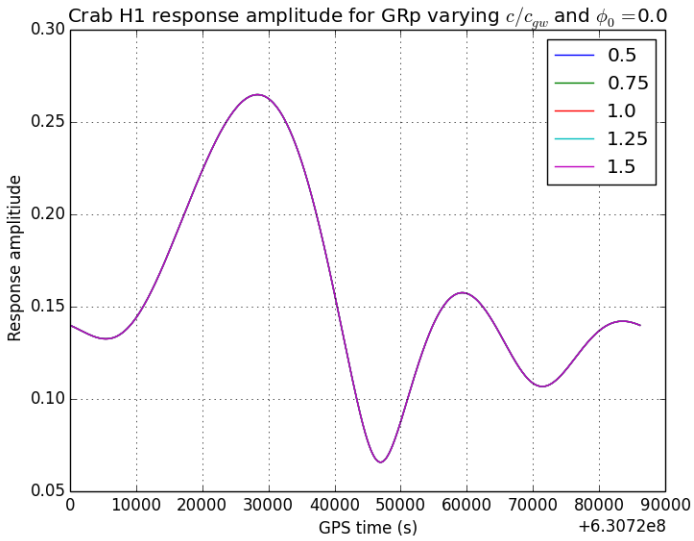

Figure 15: The amplitude modulation of the signal is unaffected by changes in GW speed, as shown by overlaying curves for all values of δ.

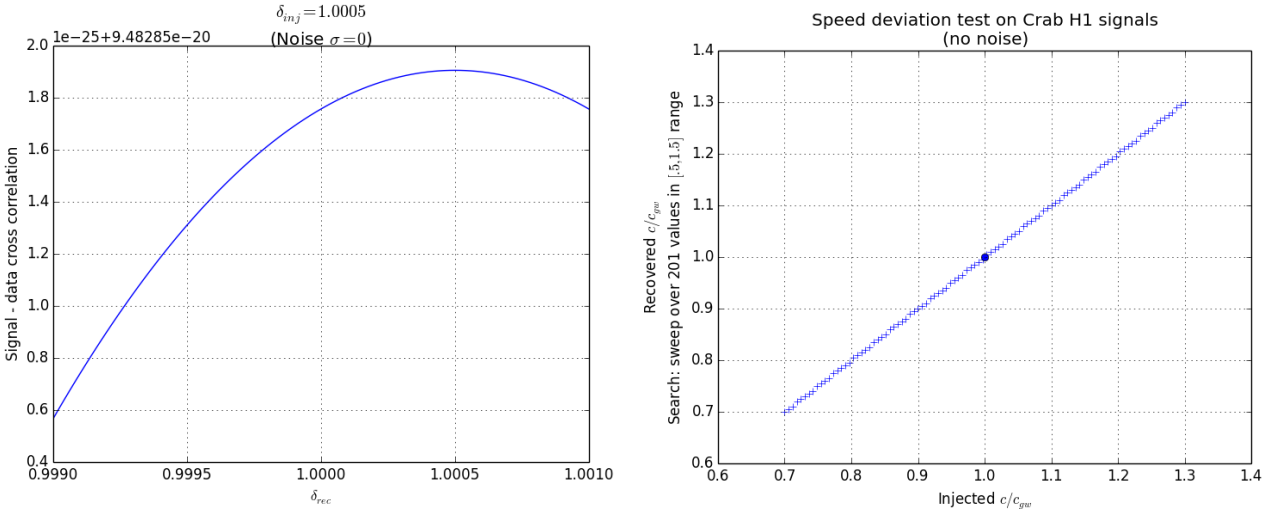

(a) $\delta_{inj} = 1.0005$

(b) $\delta_{inj} \in [0.7, 1.3]$

Figure 16: The cross-correlation between a template and a signal peaks when $\delta_{inj} = \delta_{rec}$ (left). Finding this peak we can recover δ_{inj} (right). Note that these plots are both tests performed without presence of noise.

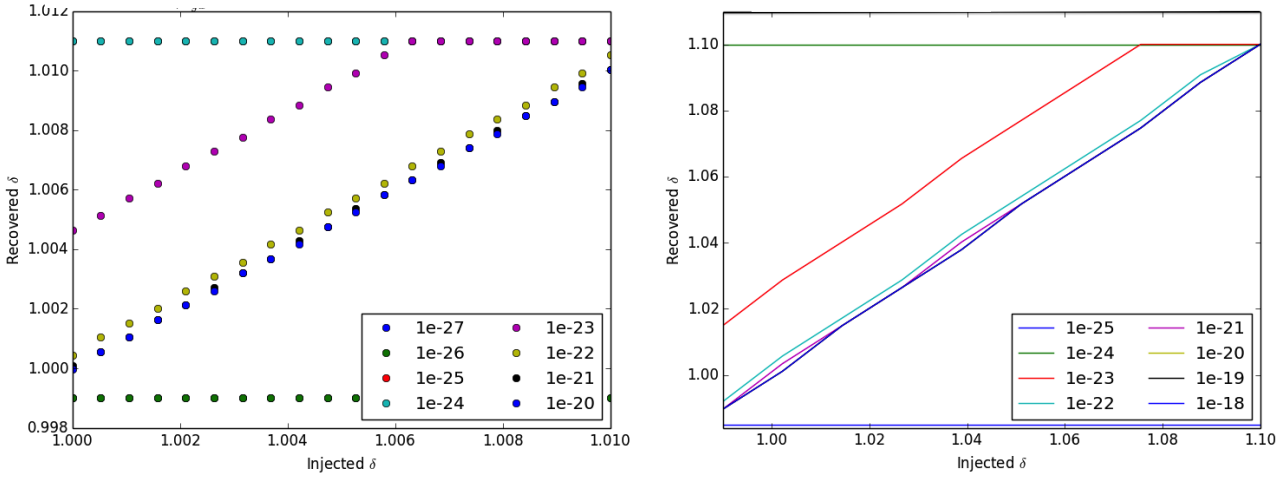

(a) Gaussian noise

(b) LIGO H1 Crab S6 noise

Figure 17: Recovered vs. injected δ for different signal strengths in Gaussian (left) and LIGO (right) noise. A slope of 1 indicates good detection. When the signal is too faint, the peak-finding makes the detection curve be a horizontal line at the maximum or minimum value of the δ_{rec} range. Note that the standard deviation of the noise is of the order 10^{-23} in both cases.

Confidence in the recovered value of δ for certain injection strength is evaluated through the root-mean-square error, i.e.

$$\text{RMSE} = \sqrt{\sum(\delta_{inj} - \delta_{rec})^2/N} \tag{45}$$

where N is the number of different injected signals (different δ_{inj}) for a given h_0. Repeating the same search multiple times but with varying noise, we obtain the uncertainty on our measurement of δ for certain SNR. For a strong signal, we are able to recover δ up to ± 0.0005 (Fig. 18a). However, when the signal is of the order of the noise, it is clear that the peak-finding procedure introduces systematic errors that push δ_{rec} towards the boundary of the search range.

4 Conclusions

We expanded our analysis of GW polarizations to include VIRGO VSR2 and VSR4 data and LIGO H1 S6 data. We reviewed the Crab pulsar, reproducing our previous results using LIGO S5 data and analyzing new LIGO S6 data. Furthermore, we looked at the Vela pulsar and 129 other pulsars in the LHO band.

We developed methods to detect GW speed variations using CGWs and we established that, for a strong enough signal, we would be able to detect deviations with a statistical error of 5×10^{-4}. More work is needed to determine if our methods can be improved when the signal diminishes in strength.

In the future, we would like to keep expanding our alternative polarizations analysis to even more pulsars, as well as refining our speed study to obtain more stringent bounds.

5 Acknowledgments

I would like to give special thanks to my mentor Dr. Alan Weinstein for his extensive support and guidance, as well as Dr. Carver Mead. I would also like to acknowledge Dr. Matthew Pitkin, without whose data this work would not have been possible. Thanks also to Dr. Kenneth Libbrecht and the Caltech SFP office.

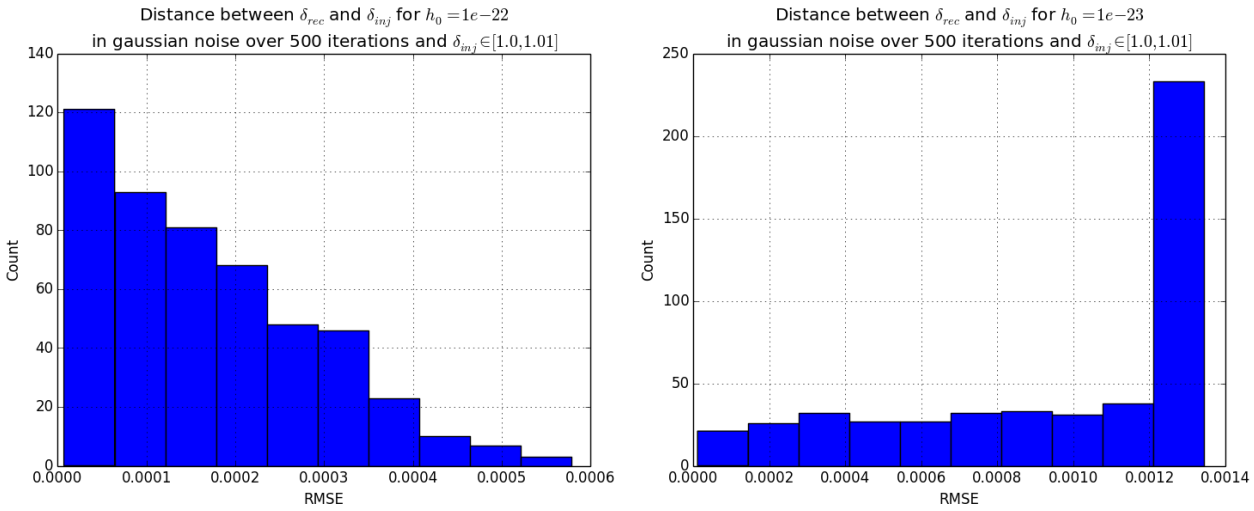

(a) $h_0 = 10^{-22}$ (b) $h_0 = 10^{-23}$

Figure 18: Histograms of RMSE for recovery of signals with $\delta \in [1.0, 1.01]$ at strong (left) and weak (right) injection strengths. For a strong signal we are able to recover δ up to ± 0.0005, while for the weak case there are clear systematic errors.

References

[1] S. G. Turyshev, Phys.-Usp., **52**, 1 (2009).

[2] B. P. Abbott et al. (The LIGO Scientific Collaboration, The Virgo Collaboration), Astrophys. J., 713, 1 (2010).

[3] A. J. Weinstein, Class. Quantum Grav. **29**, 124012 (2012).

[4] C. M. Will, Living Rev. Relativity, **9**, 3 (2006). Online Article: cited September 25, 2013, `http://www.livingreviews.org/lrr-2006-3`

[5] C. Mead, "Gravity Waves"; February 26, 2012 (unpublished).

[6] M. D. Pitkin, "Searches for Continuous and Transient Gravitational Waves from Known Neutron Stars and Their Astrophysical Implications", University of Glasgow (2006).

[7] P. Jaranowski et al, Phys. Rev. D, **58**, 063001 (1998).

[8] A. J. Weinstein, "Computing amplitude response of GW detector to different polarizations"; April 1, 2001 (unpublished).

[9] LIGO Algorithm Library routines: LalDetector, XLALComputeDetAMResponseExtraModes, XLALGreenwichMeanSiderealTime.

[10] R. J. Dupuis, G. Woan, Phys. Rev. D, **72**, 102002 (2005).

[11] M. Isi et al., "Distinguishing Polarizations in Continuous Gravitational Waves"; November 16, 2012 (DCC LIGO-G1201188-v3).

[12] M. Isi, A. J. Weinstein, "Alternative GW Polarizations in CWs: Open Boxes"; October 24, 2012 (DCC LIGO-G1200876-v2)

[13] Australia Telescope National Facility Online Pulsar Catalogue `http://www.atnf.csiro.au/research/pulsar/psrcat/`.

[14] C.-Y. Ng et al., Astrophys J. **673**, 411 (2008).

[15] B. P. Abbott et al. (The LIGO Scientific Collaboration, The Virgo Collaboration), Ap. J. Lett., 737, 93 (2011).

[16] A. G. Lyne et al., Mon. Not. R. Astron. Soc. **265**, 1003 (1993).

[17] J. Beringer et al. (Particle Data Group), Phys. Rev. D. **86**, 010001 (2012).

[18] A. S. Goldhaber, M. M. Nieto, Rev. Mod. Phys. **82**, 939 (2010).

[19] R. T. Edwards et al., Mon.Not.Roy.Astron.Soc. **372** 1549 (2006).

[20] A.W. Irwin, T. Fukushima , A & A, **348**, 642 (1991).

[21] LIGO Algorithm Library routines: XLALBarycenter.

[22] C. Lee, "Testing General Relativity using Gravitational Waves from Spinning Neutron Stars"; May 9, 2012 (DCC LIGO-T1200206-v1).

[23] J.D. Giorgini et al., "JPL's On-Line Solar System Data Service", Bull. Am. Astron. Soc. **28**(3), 1158 (1996). `http://ssd.jpl.nasa.gov/?horizons`.

[24] G. Hobbs et al., Mon. Not. Roy. Astron. Soc. **360**, 974 (2005).